PHYSICAL REVIEW D **88,** 023506 (2013)

Embedding the 125 GeV Higgs boson measured at the LHC in an effective MSSM: Possible implications for neutralino dark matter

S. Scopel,[1,*] N. Fornengo,[2] and A. Bottino[2]

[1]*Department of Physics, Sogang University, 121-742 Seoul, Korea*
[2]*Dipartimento di Fisica, Università di Torino and Istituto Nazionale di Fisica Nucleare, Sezione di Torino via P. Giuria 1, I-10125 Torino, Italy*

(Received 29 April 2013; published 3 July 2013)

We analyze the phenomenological consequences of assuming that the 125 GeV boson measured at the LHC coincides with one of the two *CP*-even Higgs bosons of an effective minimal supersymmetric extension of the Standard Model at the electroweak scale. We consider the two ensuing scenarios and discuss critically the role of the various experimental data (mainly obtained at colliders and at B factories) which provide actual or potential constraints to supersymmetric properties. Within these scenarios, properties of neutralinos as dark matter particles are analyzed from the point of view of their cosmological abundance and rates for direct and indirect detections.

DOI: 10.1103/PhysRevD.88.023506 PACS numbers: 95.35.+d, 11.30.Pb, 12.60.Jv, 95.30.Cq

I. INTRODUCTION

It is remarkable that the neutral boson with a mass of 125–126 GeV, measured at the LHC in the diphoton, ZZ, WW and $\tau\tau$ channels (hereafter denoted by H_{125}) [1], can be interpreted as the Higgs particle of the Standard Model (SM). However, due to the well-known problems of quadratic divergences related to the Higgs mass, a pressing question is whether this newly discovered Higgs-like particle can be interpreted within a supersymmetric extension of the SM, where the problem of divergences would be solved by boson-fermion loop cancellations. Should this be the case, a very rich and intriguing phenomenology would open up [2–17].

Here we investigate this possibility in detail, also in connection with possible implications for supersymmetric candidates of dark matter (DM) in the Universe. We employ a simple supersymmetric model, which we already used in previous analyses [8,18–20], consisting of an effective minimal supersymmetric extension of the Standard Model (MSSM) at the electroweak (EW) scale, where the usual hypothesis of gaugino mass unification at the scale of Grand Unification of a supergravity model, is removed; this effective MSSM is very manageable, since it is expressible in terms of a limited number of independent parameters.

The Higgs sector of this MSSM has two Higgs doublets, which generate, by spontaneous symmetry breaking, two vacuum expectation values (VEVs): v_1 and v_2. These provide masses to the down-type quarks and the up-type quarks, respectively. As usual, an angle β is introduced and defined as $\tan\beta = v_2/v_1$. This Higgs sector contains three neutral bosons: two CP even, h, H, and one CP odd, A. The two CP-even Higgs bosons are defined, in terms of the neutral components of the original Higgs doublets, as $H = \cos\alpha H_1^0 + \sin\alpha H_2^0$, $h = -\sin\alpha H_1^0 + \cos\alpha H_2^0$. In the diagonalization of their mass matrix, the mass hierarchy $m_h < m_H$ is imposed, and the angle α is taken in the range $[-\pi/2, \pi/2]$.

The lower bound on m_h can be established using the LEP data on the search for Higgs particles [21]. Contrary to the usual assumption (employed in most of the literature until very recently) of taking for this lower limit the *Standard Model* bound $m_h > 114$ GeV, in our previous works (and in the present one) we take the actual LEP constraint on the Higgs production cross sections, which can be translated into a bound on the quantity $\sin^2(\alpha - \beta)$ as a function of m_h. (This quantity represents the ratio of the cross section for the Higgs-strahlung process $e^+e^- \to Zh$ to the corresponding SM cross section; a complementary bound arises from the process $e^+e^- \to ZA$, and it is also taken into account.) In Refs. [8,18–20] we showed that the LEP limit actually allows the mass m_A to reach values as low as 90 GeV in some regions of the supersymmetric parameter space in MSSM, where the phenomenology of neutralino DM is particularly interesting.

The ATLAS and CMS data exclude the possibility that the boson A can be identified with the new particle H_{125}, but we are left with the two options: either $H \equiv H_{125}$ (hereafter denoted as scenario I) or $h \equiv H_{125}$ (scenario II).

As pointed out in Ref. [8], scenario I arises naturally in the supersymmetric scheme considered in Refs. [18–20], when m_h is taken to be as light as possible (compatibly with the mentioned LEP bound). In fact, in this regime one has $m_h \sim m_A \simeq$ (90–100) GeV, and $m_H \simeq$ (115–130) GeV [8]. This scenario has also been discussed in Refs. [4,9,12,13,15]. As remarked in Refs. [12,22], the light h boson of this scenario could be the origin of the small excess of Higgs-like events observed at LEP [23].

The second option is represented by scenario II: this scenario occurs when the Higgs-like boson observed at LHC is identified with the lighter CP-even boson h within the MSSM [2–7,9–11,13–16]. In this case,

*Corresponding author.
scopel@sogang.ac.kr

$m_h \simeq (125–126)$ GeV, and A, H can also decouple substantially from h, but with $m_A \simeq m_H$.

In this paper we analyze separately scenarios I and II, critically discussing the role of the various experimental data (mainly obtained at colliders and at B factories) which provide actual or potential constraints to supersymmetric properties. For each scenario, the properties of neutralinos as DM particles are then analyzed from the point of view of their cosmological abundance and rates for direct and indirect detections.

The scheme of the presentation is the following: In Sec. II the features of the employed MSSM are described, and in Sec. III a full list of conceivable constraints on the model is introduced. Results are given in Secs. IV, V, and VI, and conclusions in Sec. VII.

II. EFFECTIVE MSSM

The supersymmetric model we consider here is an effective MSSM scheme at the electroweak scale, with the following independent parameters: M_1, M_2, M_3, μ, $\tan\beta$, m_A, $m_{\tilde{q}_{12}}$, $m_{\tilde{t}}$, $m_{\tilde{l}_{12,L}}$, $m_{\tilde{l}_{12,R}}$, $m_{\tilde{\tau}_L}$, $m_{\tilde{\tau}_R}$ and A. We stress that the parameters are defined at the EW scale. Notations are as follows: M_1, M_2 and M_3 are the U(1), SU(2) and SU(3) gaugino masses (these parameters are taken here to be positive); μ is the Higgs mixing mass parameter; $\tan\beta$ is the ratio of the two Higgs VEVs; m_A is the mass of the CP-odd neutral Higgs boson; $m_{\tilde{q}_{12}}$ is a squark soft mass common to the squarks of the first two families; $m_{\tilde{t}}$ is the squark soft mass for the third family; $m_{\tilde{l}_{12,L}}$ and $m_{\tilde{l}_{12,R}}$ are the slepton soft masses common to the L, R components of the sleptons of the first two families; $m_{\tilde{\tau}_L}$ and $m_{\tilde{\tau}_R}$ are the slepton soft masses of the L, R components of the slepton of the third family; and A is a common dimensionless trilinear parameter for the third family, $A_{\tilde{b}} = A_{\tilde{t}} \equiv A m_{\tilde{t}}$ and $A_{\tilde{\tau}} \equiv A(m_{\tilde{\tau}_L} + m_{\tilde{\tau}_R})/2$ (the trilinear parameters for the other families being set equal to zero). In our model, no gaugino mass unification at a Grand Unified scale is assumed, and therefore M_1 can be sizeably lighter than M_2. Notice that the present version of this framework represents an extension of the model discussed in our previous papers [18–20], where a common squark and the slepton soft mass were employed for the three families.

The linear superposition of bino $\tilde{B}$, wino $\tilde{W}^{(3)}$ and of the two Higgsino states $\tilde{H}_1{}^\circ$, $\tilde{H}_2{}^\circ$ which defines the neutralino state of lowest mass m_χ is written here as

$$\chi \equiv a_1\tilde{B} + a_2\tilde{W}^{(3)} + a_3\tilde{H}_1{}^\circ + a_4\tilde{H}_2{}^\circ. \qquad (1)$$

We assume R-parity conservation to guarantee that the lightest supersymmetric particle is stable (we consider only models where this is the neutralino).

Within our model we calculate all the quantities necessary to impose the constraints discussed in Sec. III, and the cross sections relevant for direct and indirect detection of DM neutralinos: the neutralino-nucleon cross section $\sigma^{(\mathrm{nucleon})}_{\mathrm{scalar}}$ and the thermally averaged product of the neutralino pair annihilation cross section times the relative velocity $\langle\sigma_{\mathrm{ann}}v\rangle$.

The neutralino-nucleon scattering takes contributions from (h, A, H) Higgs boson exchange in the t channel and from the squark exchange in the s channel; the A-exchange contribution is suppressed by kinematic effects. This cross section is evaluated here according to the formulas given in Ref. [24]. For the crucial coupling parameter g_d entering the Higgs boson exchange amplitude, we take its *reference* value $g_{d,\mathrm{ref}} = 290$ MeV employed in our previous papers [19,20]. We recall that this quantity is affected by large uncertainties [25], with $(g_{d,\max}/g_{d,\mathrm{ref}})^2 = 3.0$ and $(g_{d,\min}/g_{d,\mathrm{ref}})^2 = 0.12$ [19,20].

We also calculate $\langle\sigma_{\mathrm{ann}}v\rangle_{\mathrm{int}}$, which is the integral of $\langle\sigma_{\mathrm{ann}}v\rangle$ from the present temperature up to the freeze-out temperature T_f, since this quantity enters the neutralino relic abundance (and, for dominant s-wave annihilation, implies $\langle\sigma_{\mathrm{ann}}v\rangle_{\mathrm{int}} \equiv x_f\langle\sigma_{\mathrm{ann}}v\rangle$):

$$\Omega_\chi h^2 = \frac{x_f}{g_\star(x_f)^{1/2}} \frac{9.9\times10^{-28}\ \mathrm{cm^3\,s^{-1}}}{\langle\sigma_{\mathrm{ann}}v\rangle_{\mathrm{int}}}, \qquad (2)$$

where x_f is defined as $x_f \equiv m_\chi/T_f$ and $g_\star(x_f)$ denotes the relativistic degrees of freedom of the thermodynamic bath at x_f.

The values of $\Omega_\chi h^2$, as obtained from Eq. (2), are employed to exclude neutralino configurations which would provide values exceeding the upper bound for cold dark matter (CDM), $(\Omega_{\mathrm{CDM}}h^2)_{\max}$, and to rescale the local neutralino density, ρ_χ, when $\Omega_\chi h^2$ turns out to be below the lower bound for CDM, $(\Omega_{\mathrm{CDM}}h^2)_{\min}$. In the latter case, we rescale ρ_χ by the factor $\xi = \rho_\chi/\rho_0$, where ρ_0 is the total local DM density; ξ is conveniently taken to be $\xi = \min\{1, \Omega_\chi h^2/(\Omega_{\mathrm{CDM}}h^2)_{\min}\}$ [26].

In the present analysis, $(\Omega_{\mathrm{CDM}}h^2)_{\min}$ and $(\Omega_{\mathrm{CDM}}h^2)_{\max}$ are assigned the values $(\Omega_{\mathrm{CDM}}h^2)_{\min} = 0.11$, $(\Omega_{\mathrm{CDM}}h^2)_{\max} = 0.13$ to conform to the new measurements by the Planck Collaboration [27].

Since the rates of DM direct detection and those of processes due to pair annihilation (with the exclusion of processes taking place in macroscopic bodies) are proportional to ρ_χ and ρ_χ^2, respectively, in the following we will consider the quantities $\xi\sigma^{(\mathrm{nucleon})}_{\mathrm{scalar}}$ and $\xi^2\langle\sigma_{\mathrm{ann}}v\rangle$.

We calculate Higgs boson masses and production cross sections using FeynHiggs [28].

III. CONSTRAINTS

We give here a listing of requirements and constraints derived from a rich set of experimental data. In Secs. III A and III B we indicate the requirements which are essential to qualifying the model we are considering. Section III C reports other constraints which can potentially bound the physical region of the supersymmetric parameter space,

but whose implications for our model are more involved and thus possibly less compelling; we will also explicitly consider the possibility of relaxing some of them. This aspect will be discussed later on.

A. Constraints from the CERN e^+e^- collider LEP2

These constraints take into account all data on supersymmetric and Higgs boson searches [29] done at LEP2 (some of which are improved by those obtained at the Tevatron and LHC, as discussed in the next subsection), as well as the upper bound on the invisible width for the decay of the Z boson into non-Standard Model particles: $\Gamma(Z \to \chi\chi) < 3$ MeV [30,31].

B. Constraints from the Tevatron and the LHC

Bounds on searches for supersymmetry from Tevatron and LHC are implemented as schematically outlined below. The observation of a Higgs-like particle seen at the LHC imposes specific requirements on the signal strength factors for the production and decay of this boson, which have been applied as discussed below.

Signal strength factors for Higgs production/decay: In the spirit of the present analysis, in the scanning of the supersymmetric parameter space, we select configurations which satisfy the following requirements, as established by the most recent results at LHC [32]:

$$0.61 < R_{\gamma\gamma} < 1.57, \tag{3}$$

$$0.75 < R_{ZZ} < 1.47, \tag{4}$$

$$0.44 < R_{WW} < 1.24, \tag{5}$$

$$0.21 < R_{\tau\tau} < 1.90, \tag{6}$$

where the ratio $R_{\gamma\gamma}$ is defined as

$$R_{\gamma\gamma} = \frac{\sigma(p + p \to H_{125})\mathrm{BR}(H_{125} \to \gamma + \gamma)}{\sigma_{\mathrm{SM}}(p + p \to H_{125})\mathrm{BR}_{\mathrm{SM}}(H_{125} \to \gamma + \gamma)}, \tag{7}$$

and similarly for the other final states. Notice that the ranges of Eqs. (3)–(6) are 2σ intervals.

Bounds from the search for Higgs decaying to tau pairs: An upper bound in the plane m_A-tan β is obtained, in our model, in an indirect way from the data reported by the CMS Collaboration in Ref. [33]. A consistency check of our procedure has been performed by using the upper bound on the production cross section reported in Ref. [34] to obtain the corresponding upper bound in the plane m_A-tan β.

Bounds on squark masses of the first two families and on the sbottom mass: These bounds are taken from the CMS official analysis of Ref. [35].

Bounds on the stop mass: These bounds are taken from the official ATLAS analyses of Ref. [36] for heavy stops and of Ref. [37] for light stops.

Decay $\mathbf{B_s \to \mu^+ + \mu^-}$: We implement the constraint recently derived by the LHCb Collaboration in Ref. [38]:

$$1.1 \times 10^{-9} < \mathrm{BR}(B_s \to \mu^+ + \mu^-) < 6.4 \times 10^{-9}. \tag{8}$$

This is a 95% C.L. limit.

Search for the decay $\mathbf{t \to b + H^+}$:

Whenever relevant, we have adopted the ATLAS 2σ upper bound on the branching ratio $\mathrm{B}(t \to b + H^+)$ as reported in Ref. [39].

C. Constraints from B factories and from $(g-2)_\mu$ measurements

Flavor physics experiments are providing stringent bounds on many physical processes that can be sizably affected by supersymmetric virtual corrections. Here we list the most relevant ones for our analysis in the specific model we are assuming.

Measurement of the branching ratio of $b \to s + \gamma$: The rate for the branching ratio of the process $b \to s + \gamma$ is taken here as $2.89 \times 10^{-4} < \mathrm{BR}(b \to s\gamma) < 4.21 \times 10^{-4}$. This interval is larger by 25% with respect to the experimental determination [40] in order to take into account theoretical uncertainties in the supersymmetric contributions [41] to the branching ratio of the process. For the Standard Model calculation, we employ the NNLO results from Ref. [42].

Search for the decay $B \to \tau + \nu$: We use here the range $0.38 \times 10^{-4} < \mathrm{BR}(B \to \tau + \nu) < 1.42 \times 10^{-4}$ (world average at 95% C.L.) [43].

Search for the decay $B \to D + \tau + \nu$: A new range for the quantity $R(D) \equiv \mathrm{BR}(B \to D\tau\nu)/\mathrm{BR}(B \to De\nu)$ has been established by the *BABAR* Collaboration [44]: $30.0 \times 10^{-2} < R(D) < 58.8 \times 10^{-2}$ (2σ interval).

Muon anomalous magnetic moment $(g-2)_\mu$: We take the conservative 2σ range $3.1 \times 10^{-10} \leq \Delta a_\mu \leq 47.9 \times 10^{-10}$ for the deviation $\Delta a_\mu \equiv a_\mu^{\mathrm{exp}} - a_\mu^{\mathrm{the}}$ of the experimental world average of $a_\mu \equiv (g_\mu - 2)/2$ [45] from the theoretical evaluation [46]. (In the latter, we estimate the leading hadronic vacuum polarization contribution in the Standard Model by combining the two determinations estimated from e^+e^- and τ-decay data.) We evaluate the supersymmetric contributions to the muon anomalous magnetic moment within the MSSM by using the formulas in Ref. [47].

IV. SELECTION OF SUPERSYMMETRIC CONFIGURATIONS AND NEUTRALINO RELIC ABUNDANCE

Here we provide the results of our analysis for scenarios I and II, regarding the selection of supersymmetric configurations and the neutralino relic abundance. The mass interval for the LHC Higgs-like particle is taken here as $123\ \mathrm{GeV} \leq m_{H_{125}} \leq 129\ \mathrm{GeV}$.

TABLE I. Values and intervals for the MSSM parameters outlined by the LHC bounds for scenario I.

Scenario I	
$\tan\beta$	(4, 6)
μ	(1800, 2000) GeV
M_1	(40, 80) GeV
M_2	(180, 800) GeV
M_3	~2000 GeV
$m_{\tilde{q}_{12}}$	(1400, 1600) GeV
$m_{\tilde{l}}$	(1400, 1600) GeV
$m_{\tilde{l}_{12,L}}$, $m_{\tilde{l}_{12,R}}$	~500 GeV
$m_{\tilde{\tau}_L}$, $m_{\tilde{\tau}_R}$	(120, 200) GeV
m_A	(100, 120) GeV
$\lvert A\rvert$	(2.5, 2.8)

A. Scenario I: $H \equiv H_{125}$

This scenario is defined by identifying the heavier CP-even Higgs neutral boson H of the MSSM with the LHC Higgs-like particle, i.e. $H \equiv H_{125}$. This implies that the mass interval for H_{125} obtained at the LHC has to be attained by H (123 GeV $\leq m_H \leq$ 129 GeV), and this entails $m_h \sim m_A \simeq$ (90–100) GeV, as already noted above. The LHC constraints on the production rates in the various channels detailed in Eqs. (3)–(6) select the sector of supersymmetric parameter space reported in Table I.[1]

The most peculiar feature of this region is represented by the high values of the parameter μ, a property which agrees with the findings of Refs. [4,13,15] and appears to be related to the constraint imposed by Eq. (3) on $R_{\gamma\gamma}$, as remarked in Ref. [13]. We also notice that the sector of parameter space defined in Table I has some similarities with the scenario denoted by *low* M_H in Ref. [15], though it differs in one important feature: in our case the slepton masses (most notably the mass parameters for $\tilde{\tau}_L$ and $\tilde{\tau}_R$) are significantly lower. These are the prerequisites for having configurations where the neutralino relic abundance does not exceed the cosmological bound.

The properties of the solutions we have found are displayed in Figs. 1–4. In Fig. 1 we show the signal strength factors for Higgs production and decay at the LHC; we notice how a sizable subset of our population of supersymmetric configurations fits quite well all LHC data on these factors. This population satisfies also the other relevant constraints from colliders, as depicted in panels (a)–(c) of Fig. 2. Panel (d) of Fig. 2 instead shows that predictions for BR($b \to s + \gamma$) and $(g-2)_\mu$ in

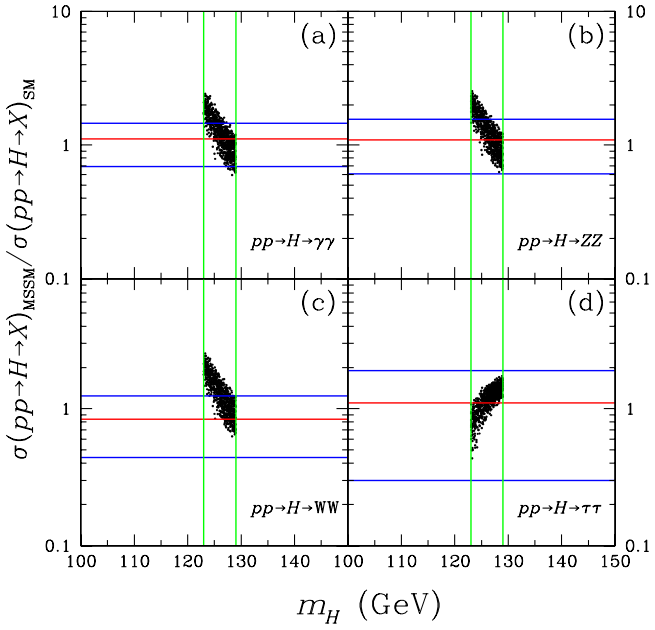

FIG. 1 (color online). Scenario I: Signal strength factors as defined in Eq. (7) for the production and decay of the heavy Higgs H when 123 GeV $\leq m_H \leq$ 129 GeV. (a) $R_{\gamma\gamma}$, (b) R_{ZZ}, (c) R_{WW}, (d) $R_{\tau\tau}$. The horizontal lines denote the allowed intervals obtained at the LHC and given in Eqs. (3)–(6).

scenario I deviate from the experimental bounds discussed in Sec. III C. A minimal deviation occurs for $(g-2)_\mu$, whereas a deviation of about 4σ occurs for BR($b \to s + \gamma$). Therefore, scenario I, which is perfectly viable as far as accelerator data are concerned, is in tension with the experimental bounds when flavor physics determinations are also included. (This will not be the case for scenario II, as discussed below.) Contrary to accelerator physics constraints, these are indirect bounds and rely to some degree on the cancellation of various terms [20], which may not be fully under theoretical control. We therefore discuss the implications of scenario I for dark matter, nevertheless reminding the reader that this scenario exhibits a significant level of tension with indirect bounds on supersymmetry.

In the present scenario the neutralino mass sits in the range $m_\chi \simeq$ (40–85) GeV. As shown in Fig. 3, most of our configurations have a sizable neutralino relic abundance. Figure 4 illustrates the contributions of different annihilation channels to the integrated cross section $\langle\sigma_{\rm ann} v\rangle_{\rm int}$; we notice that, as anticipated, light sleptons are instrumental in keeping the annihilation cross section large enough to comply with the experimental upper bound on $\Omega_\chi h^2$, since diagrams with exchange of a slepton dominate $\langle\sigma_{\rm ann} v\rangle_{\rm int}$ over the whole range of the available neutralino masses, with the exception of a small mass range around $m_\chi \simeq m_A/2$, where resonant annihilation through A exchange can become important. On the other hand, Z-boson exchange remains subdominant even close to the pole in the corresponding annihilation cross section, $m_\chi \simeq M_Z/2$,

[1]For the lower bound on the slepton masses, we use here the LEP values $m_{\tilde{l}} \gtrsim$ 80–100 GeV (depending on flavor) [31]. These lower bounds actually depend on the condition that $m_{\tilde{l}} - m_{\chi_1} > O$(3–15) GeV. If these conditions are not met, the slepton lower bound can decrease to about 40 GeV, with relevant implications for the neutralino phenomenology, as discussed in Ref. [48].

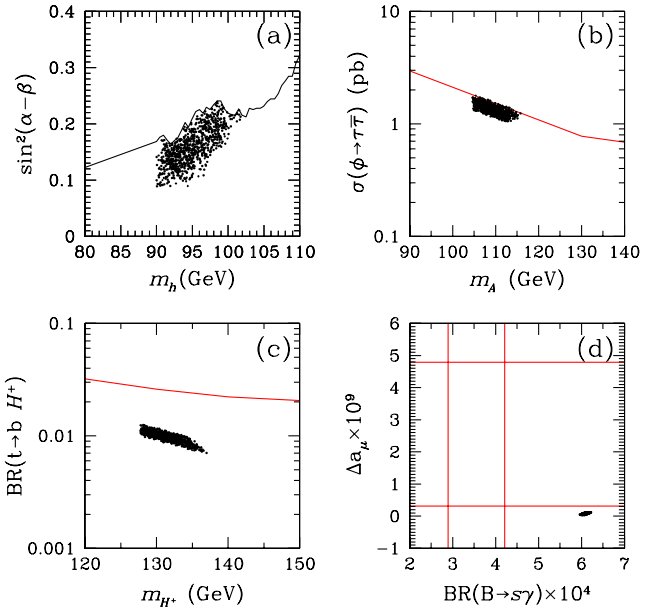

FIG. 2 (color online). Scenario I: Some of the experimental constraints discussed in Sec. III are compared to the corresponding theoretical expectations for the supersymmetric configurations reported in Table I and Fig. 1. Panels (a)–(c) correspond to collider constraints: (a) LEP bound on the Higgs production cross section, reported in terms of the coupling factor $\sin^2(\alpha-\beta)$ [29]. (b) CMS bound on Higgs production and subsequent decay into $\tau\bar{\tau}$ [33]. (The production cross section refers to $\phi = A$ unless $m_A \simeq m_h$ or $m_A \simeq m_H$, in which case $\phi = A$, h or $\phi = A$, H, respectively.) (c) ATLAS upper bound on the branching ratio $\mathrm{BR}(t \to bH^+)$ [39]. Panel (d) shows the extent of deviations from the two constraints on $\mathrm{BR}(b \to s+\gamma)$ and $(g-2)_\mu$.

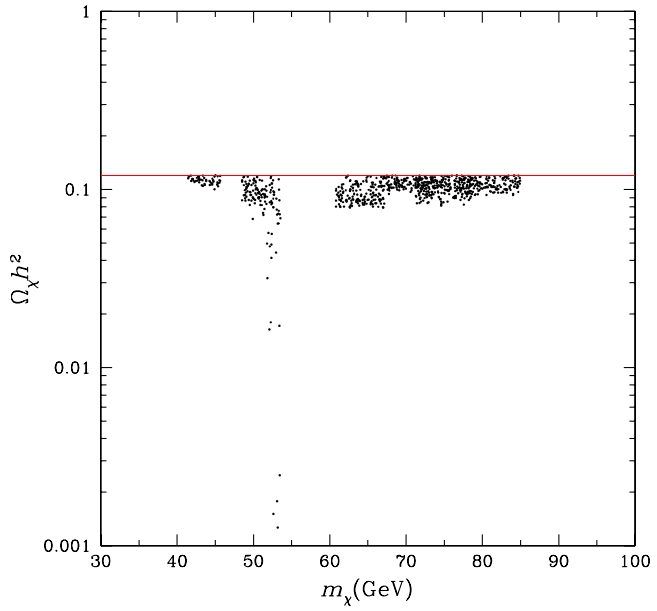

FIG. 3 (color online). Scenario I: Neutralino relic abundance as a function of the neutralino mass for the supersymmetric configurations reported in Table I and Fig. 1. The horizontal line represents the upper bound $(\Omega_{\mathrm{CDM}}h^2)_{\mathrm{max}} = 0.13$ from the Planck Collaboration [27] on the cold dark matter content in the Universe.

since the Z boson couples to the neutralino only through its Higgsino components, while in this scenario the neutralino is a bino of extremely high purity, due to the very large values required for the μ parameter, as specified in Table I. Finally, for the same set of supersymmetric configurations we show in Fig. 5 the ratios $[\langle\sigma_{\mathrm{ann}}v\rangle_i/\langle\sigma_{\mathrm{ann}}v\rangle_{\mathrm{tot}}]_{T=0}$ between the neutralino annihilation cross sections times velocity to the final states $i = \tau\tau$, $b\bar{b}$ and the total annihilation cross section times velocity, both calculated at zero temperature. The latter quantities are relevant for the evaluation of indirect signals, as discussed in Sec. VI. As shown in the plot, annihilation to $\tau\bar{\tau}$ (driven by the exchange of light staus) is dominant, with a subdominant contribution from the $b\bar{b}$ annihilation channel (which, as in the case of $\langle\sigma_{\mathrm{ann}}v\rangle_{\mathrm{int}}$, can become sizeable through resonant annihilation through A exchange).

B. Scenario II: $h \equiv H_{125}$

This scenario is defined by the alternative choice that identifies the lighter CP-even Higgs neutral boson h of the MSSM with the LHC Higgs-like particle, i.e. $h \equiv H_{125}$. This therefore implies 123 GeV $\leq m_h \leq$ 129 GeV. The scan of the MSSM parameter space that produces a

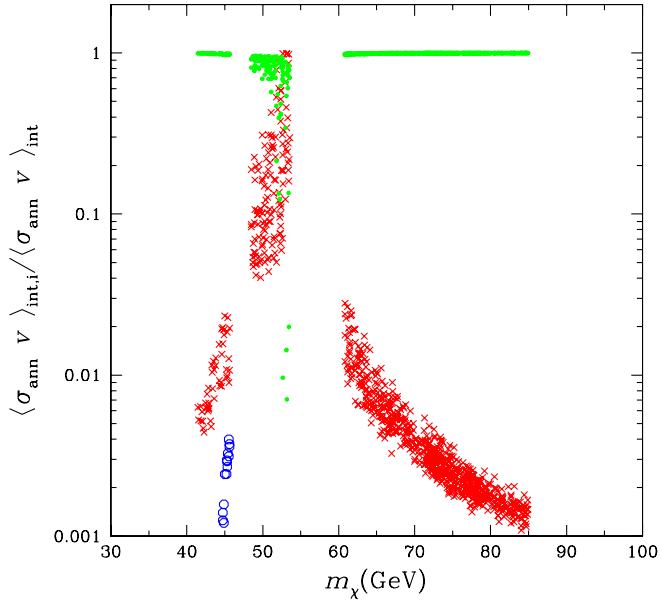

FIG. 4 (color online). Scenario I: Fractional contributions of different annihilation channels to the integrated neutralino cross section times velocity $\langle\sigma_{\mathrm{ann}}v\rangle_{\mathrm{int}}$ for the supersymmetric configurations reported in Table I and Fig. 1. Green dots: $\chi\chi \to f\bar{f}$ through slepton exchange. Red crosses: $\chi\chi \to f\bar{f}$ through Higgs exchange. Blue open circles: $\chi\chi \to f\bar{f}$ through Z boson exchange.

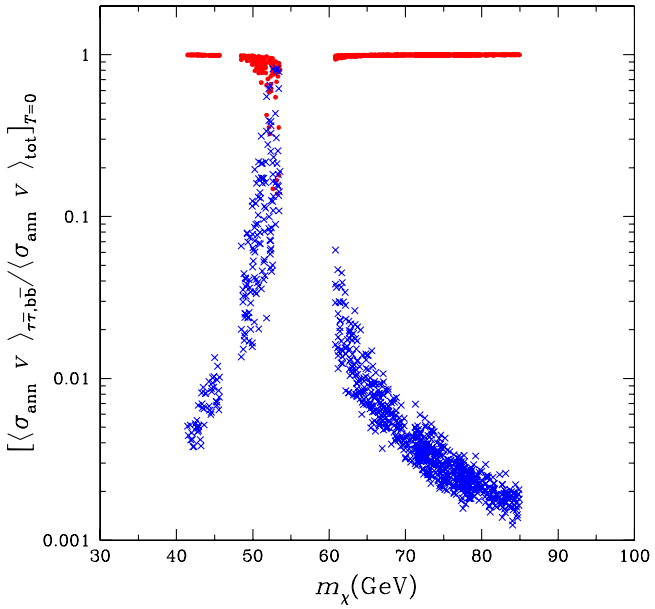

FIG. 5 (color online). Scenario I: Ratios $[\langle\sigma_{ann}v\rangle_i/\langle\sigma_{ann}v\rangle_{tot}]_{T=0}$ between the neutralino annihilation cross sections times velocity to the final states $i = \tau\tau$, $b\bar{b}$ and the total annihilation cross section times velocity, both calculated at zero temperature, for the supersymmetric configurations reported in Table I and Fig. 1. Red dots: $\tau\bar{\tau}$ final state. Blue crosses: $b\bar{b}$ final state.

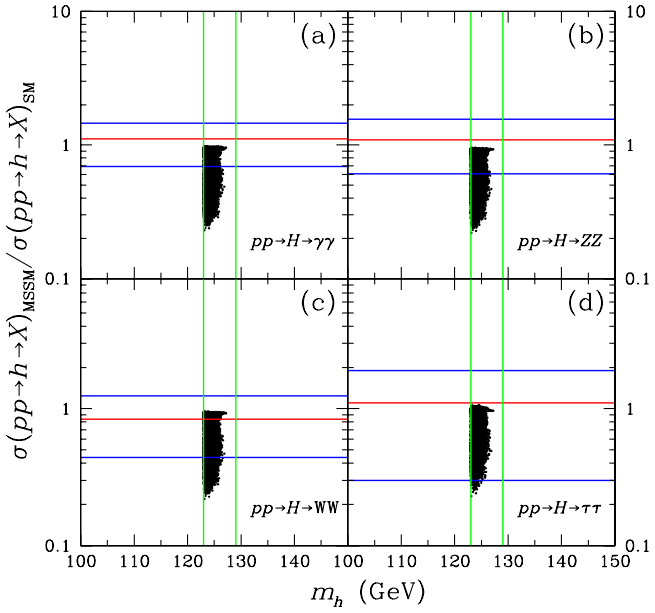

FIG. 6 (color online). Scenario II: The same as in Fig. 1, except that here 123 GeV $\leq m_h \leq$ 129 GeV.

population of configurations satisfying all requirements and constraints mentioned in Sec. III identifies the sector outlined in Table II. The features of this population are displayed in Figs. 6–10.

Figure 6 shows how the requirements for the signal strength factors are verified for our configurations. The constraint derived from LHC searches for a Higgs decaying to a tau pair implies for the mass of the CP-odd Higgs A the lower bound: $m_A \gtrsim 300$ GeV, as indicated by panel (a) of Fig. 7. Figure 7(b) shows that, at variance with the previous case, in scenario II the constraints BR($b\to s+\gamma$) and $(g-2)_\mu$ are satisfied. It is also worth noting that the bound on the branching ratio for the invisible decay $h \to \chi + \chi$ [49], not explicitly discussed before, is respected.

The plot of Fig. 8, displaying the neutralino relic abundance versus the neutralino mass, shows that m_χ has the

TABLE II. Values and intervals for the MSSM parameters outlined by the LHC bounds for scenario II.

Scenario II	
$\tan\beta$	(4, 20)
$\lvert\mu\rvert$	(100, 400) GeV
M_1	(40, 170) GeV
M_2	(100, 1000) GeV
M_3	~2000 GeV
$m_{\tilde{q}_{12}}$	(700, 2000) GeV
$m_{\tilde{t}}$	(700, 1200) GeV
$m_{\tilde{l}_{12,L}}$, $m_{\tilde{l}_{12,R}}$, $m_{\tilde{\tau}_L}$, $m_{\tilde{\tau}_R}$	(80, 1000) GeV
m_A	(200, 1000) GeV
$\lvert A\rvert$	(1.5, 2.5)

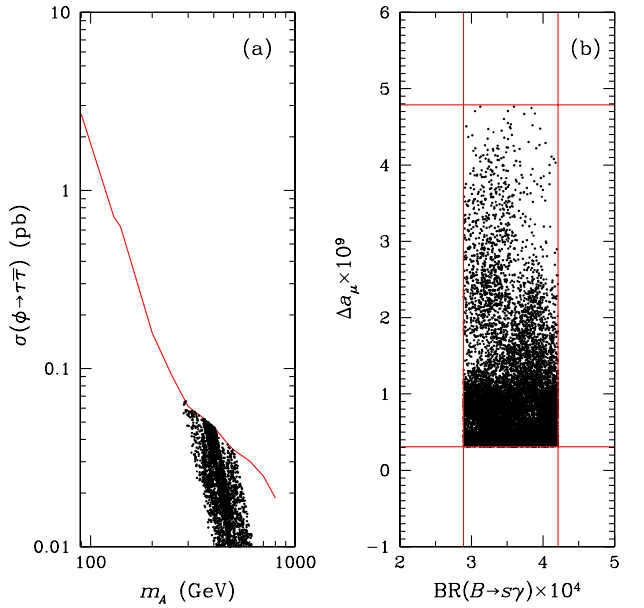

FIG. 7 (color online). Scenario II: Two of the experimental constraints discussed in Sec. III are compared to the corresponding theoretical expectations for the supersymmetric configurations reported in Table II and in Fig. 6. (a) CMS bound on Higgs production and subsequent decay into $\tau\bar{\tau}$ [33]. (The production cross section refers to $\phi = A$ unless $m_A \simeq m_h$ or $m_A \simeq m_H$, in which case $\phi = A$, h or $\phi = A$, H, respectively.) (b) The two constraints on BR($b \to s + \gamma$) and $(g-2)_\mu$, which in this scenario are simultaneously satisfied.

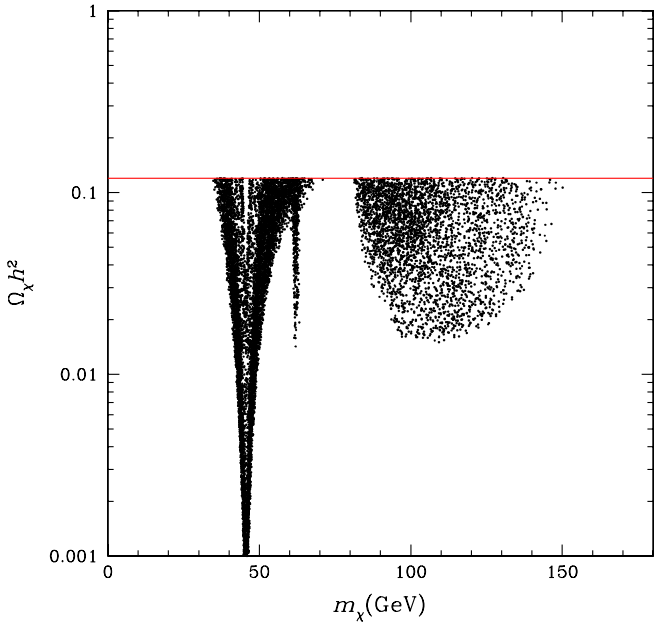

FIG. 8 (color online). Scenario II: The same as in Fig. 3, for the supersymmetric configurations reported in Table II and in Fig. 6.

lower limit $m_\chi \gtrsim 30$ GeV and that there exists a break in the range 70 GeV $\lesssim m_\chi \lesssim$ 85 GeV, this interval being disallowed by the requirement that $\Omega_\chi h^2 \leq (\Omega_{\rm CDM} h^2)_{\rm max}$. In turn, this property is due to the strong enhancement in

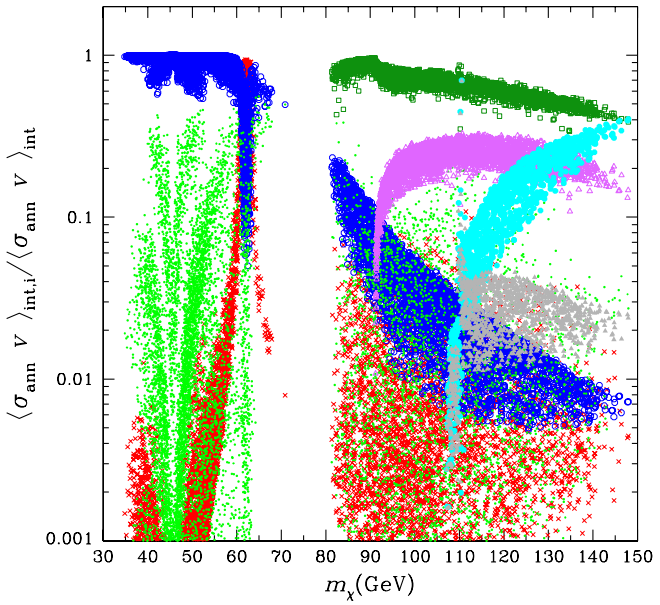

FIG. 9 (color online). Scenario II: The same as in Fig. 4, for the supersymmetric configurations reported in Table II and in Fig. 6. Green dots: $\chi\chi \to f\bar{f}$ through slepton exchange. Red crosses: $\chi\chi \to f\bar{f}$ through Higgs exchange. Blue open circles: $\chi\chi \to f\bar{f}$ through Z-boson exchange. Dark green open squares: $\chi\chi \to WW$. Purple open triangles: $\chi\chi \to ZZ$. Cyan filled circles: $\chi\chi \to Zh$. Grey filled triangles: $\chi\chi \to hh$.

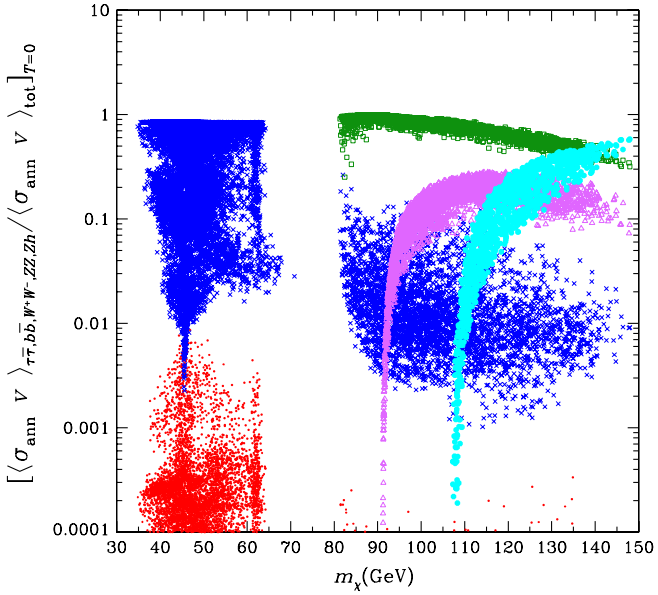

FIG. 10 (color online). Scenario II: The same as in Fig. 5, for the supersymmetric configurations reported in Table II and in Fig. 6. Red dots: $\tau\bar{\tau}$ final state. Blue crosses: $b\bar{b}$ final state. Dark green open squares: W^+W^- final state. Purple open triangles: ZZ final state. Cyan filled circles: Zh final state.

the pair annihilation amplitude when m_χ runs over the values $\frac{1}{2}m_h$, $\frac{1}{2}m_Z$.

Figure 9 displays the various contributions to $\langle \sigma_{\rm ann} v \rangle_{\rm int}$ and shows that dominances in the annihilation amplitude are as follows: (a) dominance of annihilation to fermions through Z exchange in the range 30 GeV $\lesssim m_\chi \lesssim$ 60 GeV, (b) dominance of annihilation to fermions through light scalar Higgs exchange for $m_\chi \simeq m_h/2$, and (c) dominance of annihilation to W^+W^- for $m_\chi > m_W$. To conclude the discussion, Fig. 10 shows the ratios $[\langle \sigma_{\rm ann} v \rangle_i / \langle \sigma_{\rm ann} v \rangle_{\rm tot}]_{T=0}$ between the neutralino annihilation cross section times velocity to the final states $i = \tau\tau$, $b\bar{b}$, W^+W^-, ZZ, Zh and the total annihilation cross section times velocity, both calculated at zero temperature: as shown in the plot, $\tau\bar{\tau}$ dominates when $m_\chi \lesssim 65$ GeV, W^+W^- prevails when $m_W < m_\chi < m_Z + m_h$, and Zh dominates at larger masses.

V. DIRECT DETECTION

We turn now to the evaluation of the relevant quantity for DM direct detection, $\xi\sigma_{\rm scalar}^{\rm (nucleon)}$. The values for this quantity are shown in the scatter plot of Fig. 11 together with the regions pertaining to the signals measured by the experiments of DM direct detection of Refs. [50,51]. (Other experimental results showing an excess of events compatible with a positive signal are reported in Refs. [52,53].) In particular, in Fig. 11, red crosses represent configurations found in the set of scenario I, while blue dots correspond to configurations found in scenario II.

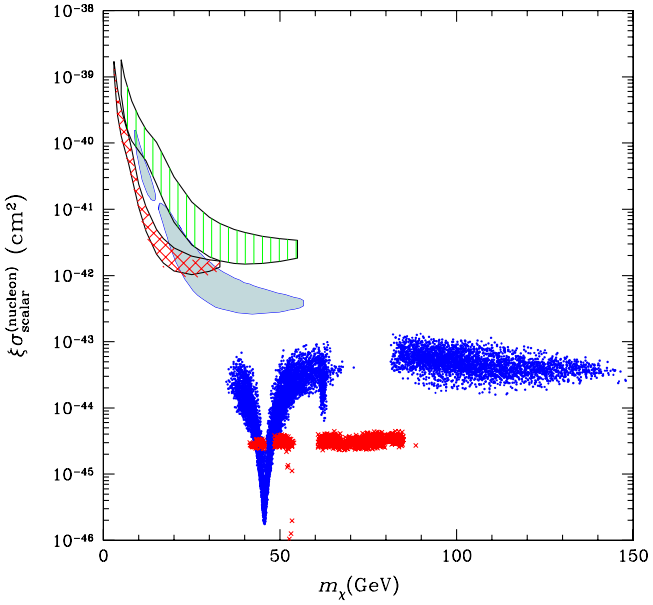

FIG. 11 (color online). Neutralino-nucleon coherent cross section times the rescaling factor $\xi\sigma^{(\mathrm{nucleon})}_{\mathrm{scalar}}$. Red crosses: supersymmetric configurations plotted in Fig. 1 (scenario I in the text). Blue dots: supersymmetric configurations plotted in Fig. 6 (scenario II in the text). The hatched areas denote the DAMA/LIBRA annual modulation regions [50]: The green vertically hatched region refers to the case where constant values of 0.3 and 0.09 are taken for the quenching factors of Na and I, respectively [54]. The red crosshatched region is obtained by using the energy-dependent Na and I quenching factors as established by the procedure given in Ref. [71]. The gray regions are those compatible with the CRESST excess [51]. In all cases a possible channeling effect is not included. The halo distribution function used to extract the experimental regions is given in the text. For other distribution functions, see Ref. [54].

The experimental domains shown here were obtained by using for the velocity distribution function of the Galactic dark matter—those pertaining to a standard isothermal sphere with $\rho_0 = 0.30$ GeV cm^{-3}, $v_0 = 220$ km sec^{-1}, with $v_{\mathrm{esc}} = 650$ km sec^{-1} for the DAMA/LIBRA experiment and $v_{\mathrm{esc}} = 544$ km sec^{-1} for CRESST and for specific sets of experimental parameters (quenching factors and others), as discussed in Refs. [50,51]. Including uncertainties of various origin, the experimental regions would expand as indicated, for instance, in Fig. 7 of Ref. [54].

One notices that the set of configurations found in scenario I generate very low rates for direct detection of relic neutralinos. Thus, in this scheme, neutralinos does not appear be responsible for the signals measured by the experiments of DM direct detection of Refs. [50–53].

It is worth stressing that these conclusions rest heavily on the results recently obtained from colliders; in particular, very constraining are the conditions expressed in Eqs. (3)–(6) and the bounds implied by the search for Higgs decay into tau pairs, that constrain the parameter μ to be very large and tan β small. Should these constraints significantly relax in the future, as a consequence of further experimental data and analyses from colliders, the theoretical values of $\xi\sigma^{(\mathrm{nucleon})}_{\mathrm{scalar}}$ would compare to the data of DM direct detection much more favorably, as for instance depicted in Fig. 5 of Ref. [8].

In the case of scenario II, in view of the experimental uncertainties mentioned above and of the theoretical uncertainties related to the parameter g_d (see Sec. II), the gap between the experimental regions and the scatter plot shown in Fig. 11 could somewhat narrow down. Most of the theoretical values shown in Fig. 11 are in tension with the experimental bounds given by other DM experiments (see for instance Refs. [55,56]).

VI. INDIRECT DETECTION

In order to study the capability of indirect signals to probe neutralino dark matter in scenario I and scenario II, we discuss the exotic component in cosmic rays represented by antiprotons, and the contribution to the so-called isotropic gamma-ray background (IGRB) due to the production of gamma rays at high latitudes from annihilation in our Galaxy.

Antiprotons are potentially able to provide quite strong bounds on dark matter annihilation in our Galaxy. We therefore calculate the antiproton production in both scenarios and compare them with the PAMELA measurements of the absolute antiproton flux [57]. Similar bounds can be obtained with the BESS–Polar II determination [58]. Figure 12 shows the antiproton fluxes in the first PAMELA energy bin ($T_{\bar{p}} = 0.28$ GeV) for the configurations of scenario I (red crosses) and scenario II (blue circles). The left panel refers to a Galactic propagation model with the MED values of propagation parameters [59]; the right panel refers to the MAX set of parameters [59]. The MAX set refers to the configuration in the space of propagation parameters which provides the largest antiproton fluxes (mostly due to a large volume of the cosmic ray confinement region), while being allowed by B/C measurements [59].

The upper long-dashed line denotes the 95% C.L. bound by using the PAMELA data [57] and adding in quadrature a 40% theoretical error on the theoretical determination of the antiproton background. This generous allowance is taken under consideration because of uncertainties in the nuclear cross sections relevant for the secondary production [59]. The modification of the bound when a smaller estimate of the theoretical uncertainty (20%) is adopted [59] is shown by the short-dashed line. We notice that antiprotons are far from bounding the configurations of both scenarios I and II. This is due to the fact that the dominant channel of annihilation in a large portion of the parameter space of both scenarios is a leptonic one (namely, $\tau\bar{\tau}$) which is unable to produce a relevant amount of antiprotons. Only those configurations of scenario I

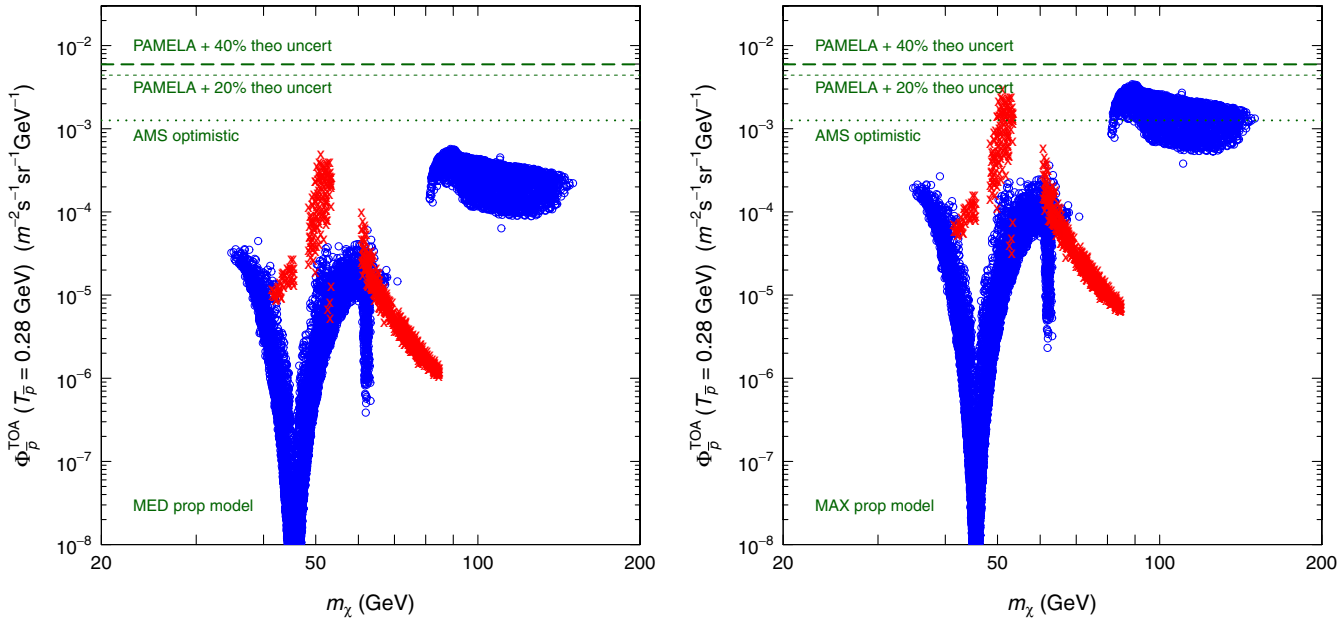

FIG. 12 (color online). Antiproton fluxes in the first PAMELA energy bin ($T_{\bar{p}} = 0.28$ GeV) for the configurations of scenario I (red crosses) and scenario II (blue circles). The upper long-dashed line denotes the 95% C.L. bound by using the PAMELA [57] data and adding in quadrature a 40% theoretical error on the theoretical determination of the antiproton background. The short-dashed line shows the same upper bound, with a 20% estimate of the theoretical uncertainty. The dotted line denotes the reaching capabilities of AMS [60], provided the total experimental and theoretical uncertainties are reduced to 10%. The left panel refers to a Galactic propagation model with the MED values of propagation parameters [59]; the right panel refers to the MAX set of parameters [59].

where the $b\bar{b}$ final state dominates (very few configurations with a neutralino mass close to 55 GeV, as seen in Fig. 5) and the configurations of scenario II where the gauge boson final state dominates (for neutralino masses above 80 GeV, as seen in Fig. 10) are able to produce an antiproton flux that reaches its maximal values. Dominant hadronic ($b\bar{b}$) final states for neutralino masses below 70 GeV are accompanied by small values of the neutralino relic abundance: this has a strong impact in reducing the antiproton flux, due to the squared appearance of the rescaling factor ξ in indirect signals (since they depend on ρ_χ^2).

Current antiproton bounds, therefore, do not constrain our supersymmetric configuration, neither for the MIN nor for the MAX set of propagation parameters. Prospects for future searches are shown in Fig. 12 by the dotted line, which refers to an expected reach of AMS [60]. We estimated AMS capabilities by taking into consideration the following facts: AMS data on antiprotons will likely reach a level of a few percent uncertainty, AMS will determine the fluxes of cosmic rays species to an unprecedented level, and this will help in reducing also the theoretical modeling of Galactic cosmic ray propagation. Determination of the boron-to-carbon (B/C) ratio will be especially relevant. By considering a total (theoretical + experimental) uncertainty on the antiproton fluxes after AMS, we can estimate a bound (in case of nonobservation of deviation from the expected background) at the level of the dotted lines in Fig. 12; this would allow us to probe a fraction of the parameter space, both for scenario I and for scenario II, in the case of relatively large values of the propagation parameters (right panel of Fig. 12). This capability is further illustrated in Fig. 13, where two representative antiproton fluxes (one for scenario I and one for scenario II) are reported. The two fluxes refer to the best choice occurring in our parameter space, but are nevertheless representative of those configurations with fluxes in excess of the AMS reaching capabilities shown in the right panel of Fig. 12. Dark matter fluxes like those shown in Fig. 13 will easily represent a detectable signal in AMS, considering that they produce visible excesses over the background (denoted by the solid line, while the dashed lines bracket a $\pm 10\%$ uncertainty) in most of the energy spectrum. We also stress that AMS will have a very large set of statistics, and therefore an excess like those shown in Fig. 13 will be detected as a deviation in a large number of experimental bins, thus making the evidence of a signal potentially quite clear. The major limitation remains the ability to reduce the theoretical uncertainties on the background to a suitable level, as discussed above.

Concerning the indirect signal in terms of gamma rays, Fig. 14 shows the flux of gamma rays produced by Galactic dark matter annihilation at high latitudes for both scenario I and scenario II. The contribution to the IGRB has been calculated for an Einasto profile of the dark matter density, but different profiles predict only slightly different fluxes [61], since we are looking here at high Galactic latitudes.

The signal fluxes in both scenario I and scenario II are relatively small when compared to the current upper

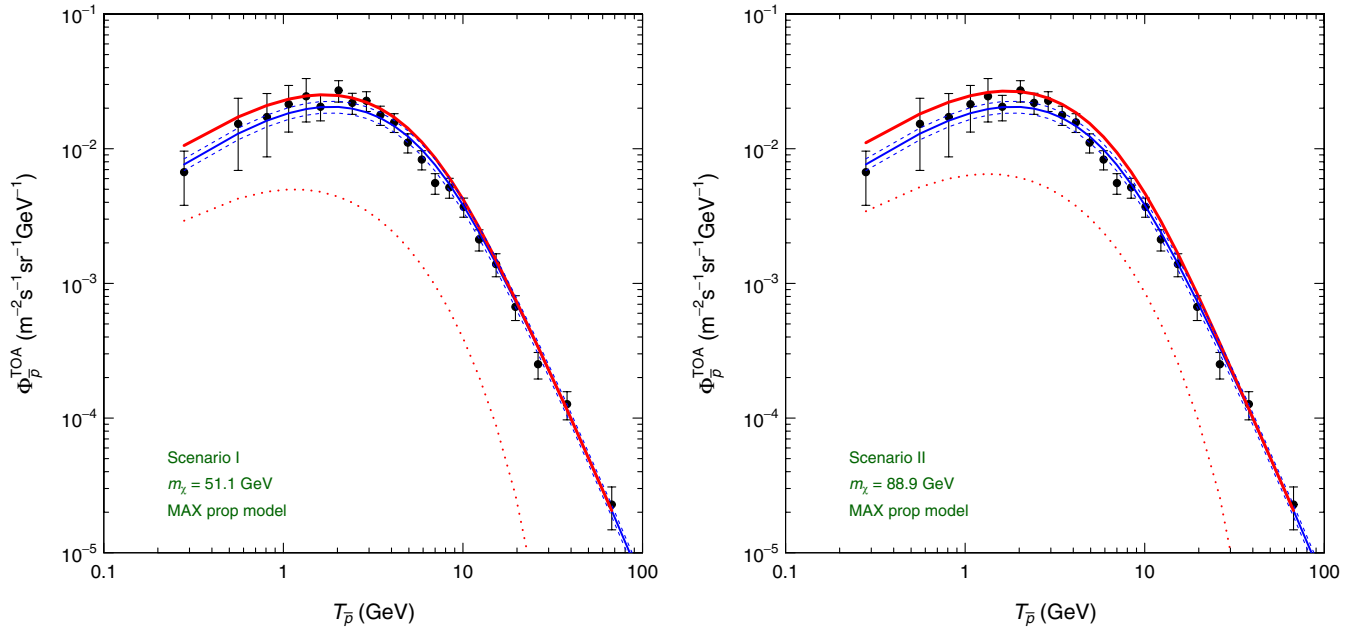

FIG. 13 (color online). Representative best antiproton fluxes for scenario I (left panel) and scenario II (right panel). Data refer to PAMELA measurement [57] of the cosmic ray antiproton flux. The lower, blue solid line refers to the theoretical determination of the secondary antiproton flux [59]. The dashed blue lines show a 10% uncertainty on the secondary determination. The dotted red line shows the signal antiproton flux produced by dark matter annihilation: the best cases are considered, and they refer to $m_\chi = 51.1$ GeV for scenario I and to $m_\chi = 88.9$ GeV for scenario II. The upper, red solid curve shows the sum of the secondary background and the signal. In both panels, the MAX set of propagation parameters is used [59].

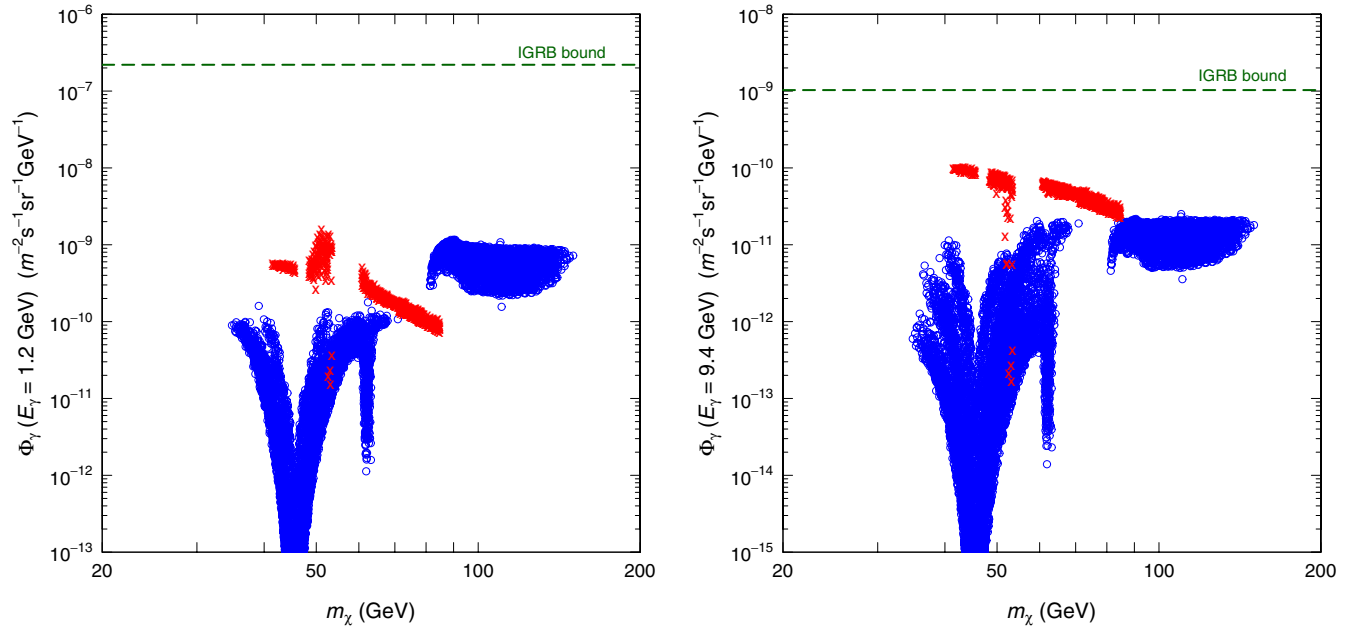

FIG. 14 (color online). Flux of gamma rays produced by Galactic dark matter annihilation at high latitudes. The horizontal dashed line represents the upper bound on the isotropic gamma-ray background (IGRB) as determined by considering the Fermi-LAT [62] measurements and the best fit of various contributions to the IGRB [61]: misaligned AGN [63], star–forming galaxies [64], unresolved millisecond pulsars [65], BL Lacertae [66] and flat-spectrum radio quasars [67]. The two panels show the fluxes in two different energy bins of the Fermi-LAT analysis [62]: the left panel refers to $E_\gamma = 1.2$ GeV, the right panel to $E_\gamma = 9.4$ GeV. Red crosses refer to configurations of scenario I; blue circles to scenario II.

bounds on the IGRB, obtained by considering the Fermi-LAT measurements [62] and the best fits of various contributions to the IGRB [61]: misaligned AGN [63], star-forming galaxies [64], unresolved millisecond pulsars [65], BL Lacertae [66] and flat-spectrum radio quasars [67]. The upper bound at the 95% C.L. is shown in Fig. 14 by the horizontal dashed line. The figure shows the flux at two representative energies, corresponding to two different energy bins of the Fermi-LAT analysis [62]: the left panel refers to $E_\gamma = 1.2$ GeV, the right panel to $E_\gamma = 9.4$ GeV.

We notice that the contribution to the IGRB of astrophysical origin suffers of large uncertainties: in deriving the bounds shown in Fig. 14 we have adopted the central-value determinations of the different sources of background, as reported in Ref. [61]. If (just) some of these background fluxes are allowed to fluctuate up (especially the recently determined gamma-ray flux originating from misaligned AGN [63]), the ensuing bounds can become quite constraining [61].

VII. CONCLUSIONS

The attempt to interpret the neutral boson (H_{125}) measured at the LHC in the diphoton, ZZ, WW and $\tau\tau$ channels, and with a mass of 125–126 GeV, in terms of the effective minimal supersymmetric extension of the Standard Model defined in Sec. II has led us to consider two possible scenarios: scenario I, where the boson H_{125} is identified with the heavier CP-even neutral boson H, and scenario II, where the boson H_{125} is identified with the lighter CP-even neutral boson h.

The supersymmetric parameter space has been analyzed also in terms of a full set of constraints derived from collider experiments, B factories, and measurements of the muon anomalous magnetic moment. The properties of the neutralino as a dark matter constituent has been analyzed in both scenarios, considering its relic abundance and direct and indirect detection rates.

We have found that in scenario I no solution for supersymmetric configurations exists, unless two indirect constraints [BR($b \to s + \gamma$) and $(g-2)_\mu$] are relaxed. If these two requirements are not implemented, solutions with a physical relic abundance are found in a region of the supersymmetric parameter space characterized by low values for the stau mass parameters, 80 GeV $\leq m_{\tilde{l}_{12,L}}$, $m_{\tilde{l}_{12,R}}$, $m_{\tilde{\tau}_L}$, $m_{\tilde{\tau}_R} \leq 200$ GeV, and high values for the μ parameter, $\mu \geq 1.8$ TeV. In the region defined in Table I, the neutralino mass turns out to sit in the range $m_\chi \simeq$ (40–85) GeV. The set of configurations found in the present scenario generate very low rates for direct detection of relic neutralinos [the quantity $\xi\sigma^{(\mathrm{nucleon})}_{\mathrm{scalar}}$ is at the level of $\xi\sigma^{(\mathrm{nucleon})}_{\mathrm{scalar}} \sim$ a few $\times\, 10^{-45}$ cm^2]. The same occurs for indirect detection signals: only antiproton searches, under some optimistic assumptions, may be able to test scenario I for neutralino masses close to 50 GeV. For this to be reachable, a somehow large cosmic ray confinement region is required, accompanied by a reduction of the total theoretical + experimental uncertainty on the antiproton flux determination at the level of about 10%. AMS [60] is expected to beat this level of precision on the antiproton data, and its measurement of the fluxes of cosmic rays species, especially B/C, could help in reducing the uncertainties on the theoretical determination, allowing us to approach the level required to study these supersymmetric populations.

In scenario II, we have found a population of configurations which satisfy all requirements and constraints mentioned in Sec. III, including the indirect bounds coming from BR($b \to s + \gamma$) and $(g-2)_\mu$. Here the lower limit for the neutralino mass is $m_\chi \gtrsim 30$ GeV. The direct detection rates are shown to be typically rather low, though they could approach the level of the signals measured by the experiments of DM direct detection [50–53] under special instances for the DM distribution, for experimental parameters and/or for a significantly large size of the neutralino-nucleon coupling. As for the indirect signals, a situation similar to scenario I occurs: under the same, somehow optimistic, assumptions discussed above, an antiproton signal in AMS may be reachable for neutralino masses above 80 GeV.

A few comments are in order here, regarding the features of the population of relic neutralinos examined in the present paper: (a) Our results apply only to the standard situation of thermal decoupling in a standard FRW cosmology; in more extended cosmological scenarios, especially those with an enhanced expansion rate of the Universe, the features of these populations are expected to be different [68–70]. (b) The relic neutralinos considered here could constitute only a part of a multicomponent DM (another component would be the one responsible for the signals observed until now in DM direct detection experiments). (c) The derivations presented in the present paper rest heavily on the results obtained at colliders: many of the analyses pertaining to these results are actually in progress, and thus some of them could be susceptible to significant modifications, with the implication of possible substantial changes in our present conclusions.

ACKNOWLEDGMENTS

We thank F. Donato and M. Di Mauro for insightful discussions on the IGRB and on its potential in bounding DM gamma-ray signals. A. B. and N. F. acknowledge the Research Grant funded by the Istituto Nazionale di Fisica Nucleare within the *Astroparticle Physics Project* (INFN Grant No. FA51). S. S. acknowledges support by the National Research Foundation of Korea (NRF) grant funded by the Korea government (MEST) (Grant No. 2012-0008534). N. F. acknowledges the support of the Spanish MICINN Consolider Ingenio 2010 Program under Grant No. MULTIDARK CSD2009-00064.

[1] ATLAS Collaboration, Phys. Lett. B **716**, 1 (2012); CMS Collaboration, Phys. Lett. B **716**, 30 (2012).
[2] L. J. Hall, D. Pinner, and J. T. Ruderman, J. High Energy Phys. 04 (2012) 131.
[3] H. Baer, V. Barger, and A. Mustafayev, Phys. Rev. D **85**, 075010 (2012).
[4] S. Heinemeyer, O. Stål, and G. Weiglein, Phys. Lett. B **710**, 201 (2012).
[5] A. Arbey, M. Battaglia, A. Djouadi, F. Mahmoudi, and J. Quevillon, Phys. Lett. B **708**, 162 (2012).
[6] P. Draper, P. Meade, M. Reece, and D. Shih, Phys. Rev. D **85**, 095007 (2012).
[7] M. Carena, S. Gori, N. Shah, and C. E. M. Wagner, J. High Energy Phys. 03 (2012) 014.
[8] N. Fornengo, S. Scopel, and A. Bottino, Phys. Rev. D **85**, 095013 (2012).
[9] N. Christensen, T. Han, and S. Su, Phys. Rev. D **85**, 115018 (2012).
[10] M. Carena, S. Gori, N. Shah, C. E. M. Wagner, and L.-T. Wang, J. High Energy Phys. 07 (2012) 175.
[11] R. Benbrik, M. Gomez Bock, S. Heinemeyer, O. Stål, G. Weiglein, and L. Zeune, Eur. Phys. J. C **72**, 2171 (2012).
[12] M. Drees, Phys. Rev. D **86**, 115018 (2012).
[13] P. Bechtle, S. Heinemeyer, O. Stål, T. Stefaniak, G. Weiglein, and L. Zeune, Eur. Phys. J. C **73**, 2354 (2013).
[14] M. Carena, S. Gori, I. Low, N. R. Shah, and C. E. M. Wagner, J. High Energy Phys. 02 (2013) 114.
[15] M. Carena, S. Heinemeyer, O. Stål, C. E. M. Wagner, and G. Weiglein, arXiv:1302.7033.
[16] T. Han, Z. Liu, and A. Natarjan, arXiv:1303.3040.
[17] J.-J. Cao, Z.-X. Heng, J. M. Yang, Y.-M. Zhang, and J.-Y. Zhu, J. High Energy Phys. 03 (2012) 086.
[18] A. Bottino, N. Fornengo, and S. Scopel, Phys. Rev. D **67**, 063519 (2003); A. Bottino, F. Donato, N. Fornengo, and S. Scopel, Phys. Rev. D **68**, 043506 (2003).
[19] A. Bottino, F. Donato, N. Fornengo, and S. Scopel, Phys. Rev. D **78**, 083520 (2008).
[20] N. Fornengo, S. Scopel, and A. Bottino, Phys. Rev. D **83**, 015001 (2011).
[21] R. Barate *et al.* (LEP Working Group for Higgs Boson Searches and ALEPH, DELPHI, L3, and OPAL Collaborations), Phys. Lett. B **565**, 61 (2003).
[22] A. Bottino, N. Fornengo, and S. Scopel, Nucl. Phys. **B608**, 461 (2001).
[23] ALEPH, DELPHI, L3, and OPAL Collaborations, Phys. Lett. B **565**, 61 (2003).
[24] A. Bottino, F. Donato, N. Fornengo, and S. Scopel, Phys. Rev. D **59**, 095003 (1999).
[25] A. Bottino, F. Donato, N. Fornengo, and S. Scopel, Astropart. Phys. **13**, 215 (2000); **18**, 205 (2002).
[26] T. K. Gaisser, G. Steigman, and S. Tilav, Phys. Rev. D **34**, 2206 (1986).
[27] P. A. R. Ade *et al.* (Planck Collaboration), arXiv:1303.5076.
[28] M. Frank, T. Hahn, S. Heinemeyer, W. Hollik, H. Rzehak, and G. Weiglein, J. High Energy Phys. 02 (2007) 047; G. Degrassi, S. Heinemeyer, W. Hollik, P. Slavich, and G. Weiglein, Eur. Phys. J. C **28**, 133 (2003); S. Heinemeyer, W. Hollik, and G. Weiglein, Eur. Phys. J. C **9**, 343 (1999); Comput. Phys. Commun. **124**, 76 (2000).
[29] A. Colaleo (ALEPH Collaboration), *SUSY 2001, Dubna, Russia*, 2001; J. Abdallah *et al.* (DELPHI Collaboration), DELPHI Report No. 2001-085 CONF 513, 2001; LEP Higgs Working Group for Higgs Boson Searches, arXiv:hep-ex/0107029; LEP2 Joint SUSY Working Group, http://lepsusy.web.cern.ch/lepsusy/.
[30] ALEPH, DELPHI, L3, OPAL, and SLD Collaborations, LEP Electroweak Working Group, SLD Electroweak and Heavy Flavour Groups, Phys. Rep. **427**, 257 (2006).
[31] J. Beringer *et al.* (Particle Data Group), Phys. Rev. D **86**, 010001 (2012).
[32] CMS Collaboration and ATLAS Collaboration, *Rencontres de Moriond 2013, QCD and High Energy Interactions, La Thuile, Italy*, 2013.
[33] CMS Collaboration, CMS Report No. PAS HIG-12-050.
[34] CMS Collaboration, CMS Report No. PAS HIG-11-029.
[35] CMS Collaboration, CMS Report No. PAS SUS-12-028.
[36] ATLAS Collaboration, Phys. Rev. Lett. **109**, 211803 (2012).
[37] ATLAS Collaboration, Eur. Phys. J. C **72**, 2237 (2012).
[38] LHCb Collaboration, Phys. Rev. Lett. **110**, 021801 (2013).
[39] ATLAS Collaboration, J. High Energy Phys. 06 (2012) 039.
[40] E. Barberio *et al.* (Heavy Flavor Averaging Group), arXiv:hep-ex/0603003.
[41] M. Ciuchini, G. Degrassi, P. Gambino, and G. F. Giudice, Nucl. Phys. **B534**, 3 (1998).
[42] M. Misiak *et al.*, Phys. Rev. Lett. **98**, 022002 (2007).
[43] Y. Yook (Belle Collaboration), ICHEP 2012.
[44] R. Godang (*BABAR* Collaboration), EPJ Web Conf. **49**, 15002 (2013).
[45] G. W. Bennet *et al.* (Muon $g-2$ Collaboration), Phys. Rev. D **73**, 072003 (2006).
[46] M. Davier, A. Hoecker, B. Malaescu, C. Z. Yuan, and Z. Zhang, Eur. Phys. J. C **66**, 1 (2010).
[47] T. Moroi, Phys. Rev. D **53**, 6565 (1996); **56**, 4424(E) (1997).
[48] C. Boehm, P. S. B. Dev, A. Mazumdard, and E. Pukartas, arXiv:1303.5386.
[49] M. Böhler, *Rencontres de Moriond 2013, QCD and High Energy Interactions, La Thuile, Italy*, 2013.
[50] R. Bernabei *et al.*, Eur. Phys. J. C **67**, 39 (2010).
[51] G. Angloher *et al.*, Eur. Phys. J. C **72**, 1971 (2012).
[52] C. E. Aalseth *et al.* (CoGeNT Collaboration), Phys. Rev. Lett. **106**, 131301 (2011); **107**, 141301 (2011).
[53] R. Agnese *et al.* (CDMS Collaboration), arXiv:1304.4279.
[54] P. Belli, R. Bernabei, A. Bottino, F. Cappella, R. Cerulli, N. Fornengo, and S. Scopel, Phys. Rev. D **84**, 055014 (2011).
[55] E. Aprile *et al.*, Phys. Rev. Lett. **109**, 181302 (2012).
[56] Z. Ahmed *et al.* (CDMS Collaboration), Phys. Rev. Lett. **106**, 131302 (2011).
[57] O. Adriani *et al.* (PAMELA Collaboration), Phys. Rev. Lett. **105**, 121101 (2010).
[58] K. Abe, H. Fuke, S. Haino, T. Hams, M. Hasegawa, A. Horikoshi, K. C. Kim, and A. Kusumoto *et al.*, Phys. Rev. Lett. **108**, 051102 (2012).
[59] F. Donato, N. Fornengo, D. Maurin, and P. Salati, Phys. Rev. D **69**, 063501 (2004).
[60] A. Kounine (AMS Collaboration), Int. J. Mod. Phys. E **21**, 1230005 (2012).

[61] F. Calore, M. Di Mauro, and F. Donato, arXiv:1303.3284.
[62] Fermi-LAT Collaboration, Phys. Rev. Lett. **104**, 101101 (2010).
[63] M. Di Mauro, F. Calore, F. Donato, M. Ajello, and L. Latronico, arXiv:1304.0908.
[64] Fermi-LAT Collaboration, Astrophys. J. **755**, 164 (2012).
[65] F. Calore, V. De Romeri, and F. Donato, Phys. Rev. D **85**, 023004 (2012).
[66] Fermi-LAT Collaboration, Astrophys. J. **720**, 435 (2010).
[67] A. K. Harding, V. V. Usov, and A. G. Muslimov, Astrophys. J. **622**, 531 (2005).
[68] R. Catena, N. Fornengo, A. Masiero, M. Pietroni, and F. Rosati, Phys. Rev. D **70**, 063519 (2004).
[69] R. Catena, N. Fornengo, M. Pato, L. Pieri, and A. Masiero, Phys. Rev. D **81**, 123522 (2010).
[70] G. B. Gelmini, Nucl. Phys. B, Proc. Suppl. **194**, 63 (2009).
[71] V. I. Tretyak, Astropart. Phys. **33**, 40 (2010).